

# Magnetic excitations in the Kitaev material $\text{Na}_2\text{IrO}_3$ studied by neutron scattering

Alexandre Bertin ,<sup>1</sup> Hengdi Zhao ,<sup>2</sup> Gang Cao ,<sup>2</sup> Andrea Piovano ,<sup>3</sup>  
Paul Steffens ,<sup>3</sup> Alexandre Ivanov ,<sup>3</sup> and Markus Braden ,<sup>1</sup>

<sup>1</sup>*Institute of Physics II, University of Cologne, 50937 Cologne, Germany*

<sup>2</sup>*Department of Physics, University of Colorado, Boulder, CO 80309, USA*

<sup>3</sup>*Institut Laue-Langevin, 71 Avenue des Martyrs, Grenoble, 38042, cedex 9, France*

(Dated: February 17, 2026)

Inelastic neutron scattering experiments with a large set of comounted  $\text{Na}_2\text{IrO}_3$  crystals reveal the low-energy magnon dispersion in this candidate material for Kitaev physics. The magnon gap amounts to  $1.7(1)$  meV and can be interpreted similarly to the sister compound  $\alpha\text{-RuCl}_3$  to stem from the zone boundaries in the antiferromagnetic zigzag structure. The neutron experiments find no evidence for low-energy excitations with ferromagnetic character, which contrasts to the findings in  $\alpha\text{-RuCl}_3$ . Our results are consistent with a recently proposed microscopic model that involves an antiferromagnetic Heisenberg nearest-neighbor exchange in  $\text{Na}_2\text{IrO}_3$  in contrast to the ferromagnetic one considered for  $\alpha\text{-RuCl}_3$ . Although the magnetic response shows the signatures of bond-directional anisotropy in both materials the different relative signs of Kitaev and Heisenberg interaction result in different deviations from the initial Kitaev model. Low-energy ferromagnetic fluctuations cannot be considered as a fingerprint of ferromagnetic Kitaev interaction.

## I. INTRODUCTION

Systems with bond-dependent exchange couplings, i.e. compass models, have attracted a lot of attention over the past decade [1]. One of the most intriguing system is the so-called Kitaev model consisting of transition-metal ( $TM$ ) spin-1/2 arranged on a honeycomb lattice. Its exact solution predicts a quantum spin liquid (QSL) phase supporting anyon Majorana excitations [2] that are relevant for quantum computing [3]. The peculiar geometry with oxygen surrounding in form of edge-sharing octahedra enforces symmetric  $90^\circ$   $TM\text{-O-}TM$  bonds and results in reduction of the Heisenberg superexchange interaction [4, 5]. In addition, strong spin-orbit coupling (SOC) acting on a low-spin-state  $d^5$  electronic configuration in an undistorted octahedral environment implies an effective spin  $j_{\text{eff}} = \frac{1}{2}$  ground state [4]. The bond-directional character of the magnetic interaction results from the Ising coupling of different effective-spin components for different nearest-neighbor  $TM\text{-}TM$  bond orientation.

The quest for materials fulfilling the Kitaev criteria started with a scarce number of candidates:  $\text{Na}_2\text{IrO}_3$  [6],  $\alpha\text{-Li}_2\text{IrO}_3$  [7], or  $\alpha\text{-RuCl}_3$  [8]. A few other 2D materials with chemical formula  $A_3\text{LiIr}_2\text{O}_6$ , extension to 3D hyperhoneycomb lattice ( $\beta\text{-Li}_2\text{IrO}_3$ ,  $\gamma\text{-Li}_2\text{IrO}_3$ ), but also  $3d$   $TM$  and  $4f$  rare-earth compounds have garnished the realm of the Kitaev physics [9–19].

For four-valent Ir in an undistorted cubic ligand field, the  $t_{2g}$  states are split because of the strong SOC into a lower filled  $j_{\text{eff}} = \frac{3}{2}$  and an upper half-filled  $j_{\text{eff}} = \frac{1}{2}$  band. The combined effect of SOC and Coulomb interaction further opens a gap in the  $j_{\text{eff}} = \frac{1}{2}$  band into upper and lower Hubbard bands, yielding a Mott insulating state, as it is observed in  $\text{Sr}_2\text{IrO}_4$  [20, 21] and in related Ruddlesden-Popper iridates [11, 12].  $\text{Na}_2\text{IrO}_3$  falls also into the category of the Mott-type topological insulator, as revealed by angle-resolved photoemission where the

insulating gap  $\Delta \approx 340$  meV is found temperature independent [22], and it is also coined a quantum spin Hall insulator due to the prediction of helical edge states [23].

$\text{Na}_2\text{IrO}_3$  crystallizes in the  $C2/m$  space group with lattice parameters  $a = 5.43$  Å perpendicular to the Ir-Ir bonds,  $b = 9.40$  Å parallel to the bonds, and  $c = 5.61$  Å,  $\beta_m = 109.04^\circ$  [24, 25]. All reciprocal-space vectors are given in reduced lattice units (r.l.u.) with respect to this lattice. Neighboring layers are shifted parallel to the  $\mathbf{a}$  axis by about one third of the  $a$  lattice constant so that the third-nearest layer lies almost perfectly above the initial one. Note that the reciprocal lattice vector  $\mathbf{b}^*$  is parallel to  $\mathbf{b}$  and has the length of  $\frac{2\pi}{b}$ , but  $\mathbf{c}^*$  is not parallel to  $\mathbf{c}$ .  $\mathbf{c}^*$  is perpendicular to the layers and has the length  $\frac{2\pi}{d}$  with  $d$  the inter-layer distance of  $\sim 5.3$  Å. Our sample unit shows domains rotated by  $\pm 120^\circ$  around  $\mathbf{c}^*$  following the  $C_3$  symmetry of a single  $\text{IrO}_3$  layer. The domain distribution is even more complex when taking the 3D stacking into account [26], but throughout this work we only discuss the 2D aspects of magnetic excitations.

$\text{Na}_2\text{IrO}_3$  undergoes a magnetic transition towards AFM order at  $T_N = 15$  K, with a magnetic propagation wavevector  $\mathbf{q}_{\text{mag}} = (0, 1, 0.5)$ . Note that this ordering breaks the translation symmetry of a single honeycomb layer. In the zigzag-type magnetic order [24, 25] moments are aligned antiferromagnetically along an Ir-Ir bond (Z bond parallel to the  $\mathbf{b}$  axis), and ferromagnetically aligned in the direction perpendicular to the Z bond (along the  $\mathbf{a}$  axis). Two neighboring honeycomb layers are coupled antiferromagnetically. Neutron diffraction finds that the magnetic moment mostly aligns along the  $\mathbf{a}$  axis [27] and amounts to  $\sim 0.2$   $\mu_{\text{B}}$  [25]. In contrast, diffuse magnetic x-ray experiments reported that the moments are canted by an angle of  $\approx 44^\circ$  towards the vertical axis [28].

Specific-heat and susceptibility measurements on  $\text{Na}_2\text{IrO}_3$  show the magnetic transition at  $T_N = 15$  K [6, 14], and a negative Curie-Weiss temperature suggests

dominant antiferromagnetic (AFM) interaction and a moderate frustration ratio. Despite the occurrence of magnetic ordering, this material could lie near the Kitaev QSL phase. Specific-heat data yielded support for the proximity of the QSL phase [29], as a broad hump at high temperature in the magnetic specific heat was interpreted in terms of spin fractionalization. Concerning the magnetic excitation spectrum, resonant inelastic x-ray spectroscopy (RIXS) observed a broad continuum persisting up to room temperature [30, 31], which is reminiscent of the low-energy continuum found in  $\alpha$ -RuCl<sub>3</sub> [32]. The corresponding dynamical structure factor was interpreted by spin-spin correlations restricted to the Kitaev interaction on the nearest-neighbors [31], while RIXS studies with higher resolution revealed a clear dispersion that gives access to the microscopic interaction parameters [33]. The bond-directional nature of the magnetic couplings has been revealed by resonant elastic x-ray measurements that probe the diffuse magnetic correlations [28] and more recently by a scattering-vector analysis of the high-energy RIXS response [34].

$\alpha$ -RuCl<sub>3</sub> is a 4d ruthenium-based candidate for Kitaev physics with similar honeycomb layers. Also this material exhibits the nearly identical antiferromagnetic zigzag magnetic structure documenting deviations from the ideal Kitaev model [8, 14, 17]. Compared to Na<sub>2</sub>IrO<sub>3</sub>,  $\alpha$ -RuCl<sub>3</sub> offers better conditions for inelastic neutron scattering (INS) experiments that are almost completely missing for Na<sub>2</sub>IrO<sub>3</sub>. Several INS studies on  $\alpha$ -RuCl<sub>3</sub> reported the dispersion of magnetic excitations [26, 32, 35–40] yielding an estimation of the relevant interaction parameters (see Ref. [41] for a recent summary). The magnetic excitations in  $\alpha$ -RuCl<sub>3</sub> strongly deviate from the expectation for a simple isotropic antiferromagnet, in particular there are low-energy ferromagnetic (FM) fluctuations indicating competition of FM and AFM ordering schemes, and at higher temperatures the excitations with FM character even dominate [26, 32, 35–40].

Over the past decade, in order to explain the magnetic order and the dispersion of magnetic excitations, the Kitaev Hamiltonian was considerably extended by Heisenberg interactions up to the 3rd-nearest neighbors,  $J_1$ ,  $J_2$  and  $J_3$ , and by further bond-directional symmetric off-diagonal terms called  $\Gamma$  and  $\Gamma'$  [5, 13, 41–45]. The commonly accepted minimal  $HKT\Gamma'$  Hamiltonian with the nearest-neighbor anisotropic interaction corresponding to the bond type  $\zeta = X, Y, Z$  is:

$$\begin{aligned} \mathcal{H}^\zeta = & \sum_{\langle i,j \rangle} \left\{ J_1 \mathbf{S}_i \mathbf{S}_j + K S_i^\alpha S_j^\alpha + \Gamma (S_i^\beta S_j^\gamma + S_i^\gamma S_j^\beta) \right. \\ & + \Gamma' (S_i^\alpha S_j^\beta + S_i^\beta S_j^\alpha + S_i^\alpha S_j^\gamma + S_i^\gamma S_j^\alpha) \Big\} \quad (1) \\ & + J_2 \sum_{\langle\langle i,j \rangle\rangle} \mathbf{S}_i \mathbf{S}_j + J_3 \sum_{\langle\langle\langle i,j \rangle\rangle\rangle} \mathbf{S}_i \mathbf{S}_j, \end{aligned}$$

where  $(\alpha, \beta, \gamma)$  are the cubic spin coordinates  $(x, y, z)$ ,  $(y, z, x)$ , and  $(z, x, y)$  for bonds  $\zeta = X, Y, Z$ , respectively. The bond-directional parameters are  $K$  the Kitaev exchange,  $\Gamma$  and  $\Gamma'$  the symmetric off-diagonal exchange terms, and  $J_{1,2,3}$  denote the Heisenberg exchange between nearest-neighbors  $(\langle \dots \rangle)$ , 2nd nearest-neighbors  $(\langle\langle \dots \rangle\rangle)$ , and 3rd nearest-neighbors  $(\langle\langle\langle \dots \rangle\rangle\rangle)$ , respectively. While there is no doubt that Na<sub>2</sub>IrO<sub>3</sub> exhibits a strong Kitaev interaction,  $K$ , it remains an open issue whether it is dominant enough to imply Kitaev physics such as the QSL state.

Here, we report on INS studies with two triple-axis spectrometers (TAS) that could overcome the absorption and sample-size issues of Na<sub>2</sub>IrO<sub>3</sub> and that reveal the low-energy part of the spin-wave dispersion in Na<sub>2</sub>IrO<sub>3</sub>. Thereby, we complement the high-energy RIXS data and we can evaluate various  $HKT\Gamma'$  parameter sets of the magnetic interaction that were proposed in the literature.

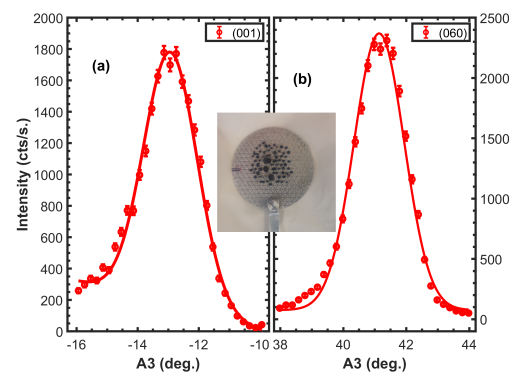


FIG. 1. Rocking scans on the nuclear reflections  $(0, 0, 1)$  (a) and  $(0, 6, 0)$  (b) measured on  $IN8(2)$ . The inset presents a photo of the 63 co-aligned Na<sub>2</sub>IrO<sub>3</sub> single crystals glued on an Aluminum plate with 30 mm diameter.

## II. EXPERIMENTAL

INS experiments were performed at the Institut Laue-Langevin (ILL, Grenoble) on the thermal neutron TAS  $IN8$  [46–48] and on the cold neutron TAS  $Thales$  [49], both equipped with focusing highly-oriented pyrolytic-graphite monochromator and analyzer units. For most scans the final neutron wavevector amounted to  $k_f = 2.662 \text{ \AA}^{-1}$  and  $1.55 \text{ \AA}^{-1}$  on  $IN8$  and  $Thales$ , respectively, resulting in an energy,  $E$ , resolution at the elastic line of  $0.2 \text{ meV}$  and  $0.8 \text{ meV}$  respectively. A pyrolytic graphite filter and a Beryllium filter were used, respectively, in order to suppress higher order contamination. On  $Thales$  a neutron velocity selector was inserted in the incoming beam. At both instruments the sample was cooled down to  $1.5 \text{ K}$  in an ILL orange-type cryostat, and we performed most scans at this temperature. Note that two different experiments have been carried out on  $IN8$  and are referred to in this manuscript as  $IN8(1)$  [47] and  $IN8(2)$  [48]. In the second  $IN8(2)$  experiment the background could be considerably reduced by improving the

positioning of diaphragms with respect to the outer walls of the cryostat.

$\text{Na}_2\text{IrO}_3$  crystals were grown using a self-flux method at University of Colorado, and similarly obtained samples were already studied in Ref. [25]. The crystals exhibit a plate shape with the large dimensions parallel to the Ir layers and with a thickness of only some tenths of mm. The crystalline quality of the crystals was analyzed by x-ray Laue diffraction. In the inset of Fig. 1 we show the sample mounting used for the INS experiments. In order to cope with the strong neutron absorption of Iridium and to obtain sufficient sample volume, 63 thin single crystals have been co-aligned and mounted with an hydrogen-free glue on an Aluminum plate. In Fig. 1(a) and (b) we show rocking scans, performed by rotating the A3 sample angle, on the  $(0, 0, 1)$  and  $(0, 6, 0)$  nuclear reflections, respectively. The full width at half maximum (FWHM) gives an estimation of the sample mosaicity  $\eta \approx 2^\circ$ , a reasonable value given the large number of co-aligned single crystals. Our sample shows the 120 degrees rotation of domains following the  $C_3$  symmetry of the single honeycomb layer. In the scattering plane spanned by  $(0, 1, 0)$  and  $(0, 0, 1)$  we avoid that neutrons pass along the larger dimensions of the individual crystals and of the total sample mounting. The absorption remains thus acceptable, but the main challenge arises from the still small size of the sample with a total mass of  $\sim 208$  mg.

Spin wave calculations using linear spin-wave theory (LSWT) have been performed with the *SpinW* package [50] implementing the magnetic-interaction model described in Equ. (1).

### III. NEUTRON SCATTERING STUDIES

#### A. Magnetic Order

Figure 2(a) illustrates the magnetic order for a single honeycomb layer, and in Fig. 2(b) and Fig. 2(c), we show elastic scans across the magnetic Bragg peak  $(0, 1, 0.5)$  taken along the in-plane  $k$  and out-of-plane  $l$  directions, respectively, on *Thales*. The Bragg peak intensities vanish above the Néel temperature  $T_N$  in agreement with previous studies [24]. Since the magnetic Bragg peak develops also along the out-of-plane component, i.e. the  $l$  direction, the order is three-dimensional. The scan profiles are fitted with Gaussian functions, and the temperature dependence of the magnetic Bragg-peak amplitudes for both scan directions, shown in Fig. 2(d), confirms  $T_N \approx 15$  K. The dashed-dotted black line is a guide to the eye, modeled with the phenomenological expression  $y = y_0 \cdot (1 - (\frac{T}{T_N})^2)^{2\beta}$ , where the square exponent accounts for the quadratic decay at low temperature of the magnetic moment due to AFM magnons, and we chose  $\beta = 0.125$ , the critical exponent of the order parameter for a 2D Ising system [52, 53]. Note, that the data density does not allow us free fitting of  $T_N$  and  $\beta$ . The FWHM is temperature independent and amounts to  $\approx 0.08$  and

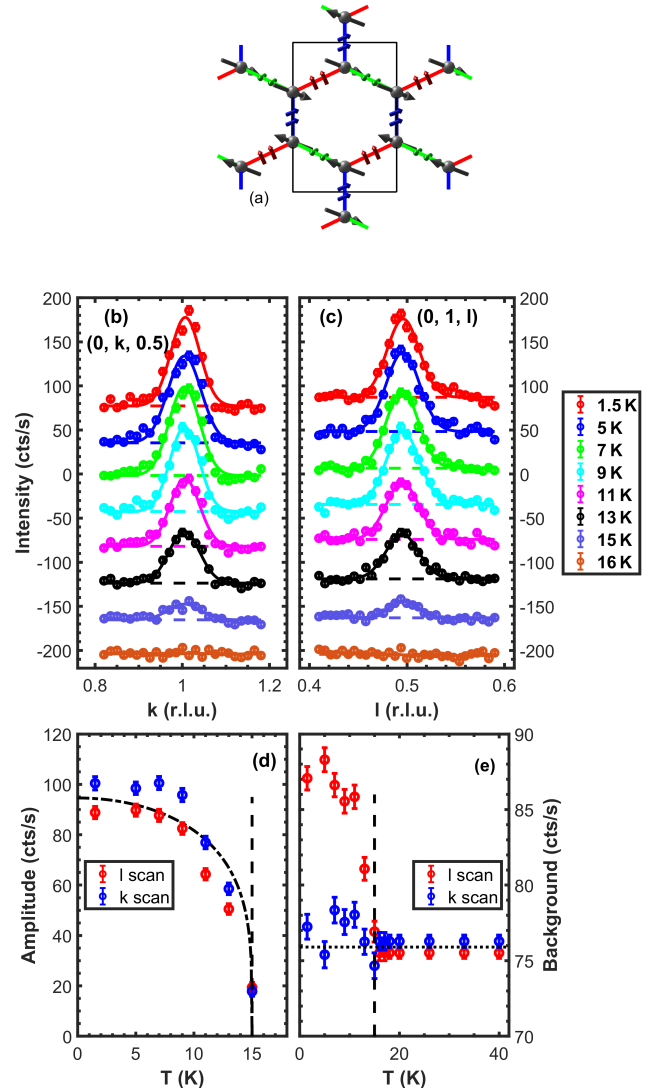


FIG. 2. (a) Scheme of the zigzag magnetic order in  $\text{Na}_2\text{IrO}_3$ : Ir sites (spheres) and ordered moments (arrows) are indicated in gray for a single honeycomb layer. The red, green and blue thick lines indicate the  $X$ ,  $Y$  and  $Z$  bonds, respectively, with the colored double arrows denoting the component ferromagnetically coupled by the Kitaev interaction acting on this bond. The monoclinic in-plane lattice parameters are shown by the black rectangle with  $a$  perpendicular and  $b$  parallel to an Ir-Ir bond. On *Thales*, we scanned the  $(0, 1, \frac{1}{2})$  magnetic Bragg peak along the  $k$  (b) and  $l$  (c) directions; some data were shifted vertically for clarity [51]. Temperature dependence of the  $(0, 1, \frac{1}{2})$  magnetic Bragg peak amplitude (d) and background (e), for both scan directions. The vertical dashed line indicates  $T_N$ . The dashed-dotted line in panel (d) is a guide to the eye, see main text. The horizontal dotted line in panel (e) indicates the paramagnetic background, averaged for both scan directions.

0.04 r.l.u. for the  $k$  and  $l$  directions, respectively, see Supplemental Material [54]. Finally, the temperature dependence of the background is shown in Fig. 2(e). While

for the  $k$  direction the background remains unaffected by the magnetic transition, a clear uptake is visible at the transition for the scans along the  $l$  direction indicative of short-range quasistatic magnetic correlations or magnetic stacking faults that emerge at the Néel temperature. This effect is sizable and indicates that analyzing the magnetic Bragg peaks will considerably underestimate the ordered moment. In contrast, we find no evidence for a persisting peak in the  $k$  scan that would indicate strong 2D quasistatic correlations above  $T_N$ .

## B. Magnetic Excitations

Despite being widely investigated, the microscopic parameters of the spin Hamiltonian remain elusive for  $\text{Na}_2\text{IrO}_3$ , because INS experiments remain scarce and only RIXS studies with an exceptional resolution can analyze the energy range of magnetic excitations in  $\text{Na}_2\text{IrO}_3$  [33]. Such experiments revealed magnetic excitations at the Brillouin zone center around 35 meV and their downward dispersion along paths into the Brillouin zone [33]. However, even with the RIXS resolution of  $\Delta E = 12$  meV it is not possible to study lowest energies of the magnetic dispersion, i.e. well below 10 meV. Inelastic neutron scattering measurements on a powder sample put an upper limit on the magnon gap  $\Delta \leq 2$  meV, and a sinusoidal-like dispersive signal at 5 meV is reported at scattering vectors,  $\mathbf{Q}$ , with short length [24] but the powder experiment cannot attribute this dispersion to a direction in reciprocal space.

We report single-crystal INS measurements aiming at mapping the low-energy spin-wave dispersion, in order to complement the high-energy data obtained by RIXS [33] and in order to evaluate the microscopic parameters of the extended  $H\text{KTF}'$  Hamiltonian defined in Eq. 1, see Sec. III C. We first describe our  $\text{Na}_2\text{IrO}_3$  experiments on the cold TAS *Thales* [49]. With the intention of resolving the energy gap  $\Delta$  at the AFM zone center  $(0, 1, 0.5)$ , we performed constant- $\mathbf{Q}$  scans on *Thales* that show the emergence of a low-energy magnon mode at  $\Delta = 1.7(1)$  meV in the ordered phase at 1.5K. This finite-energy signal vanishes above  $T_N$ , see Fig. 3(a). Slightly above the transition, at 18K, one recognizes enhanced quasi-elastic critical scattering that becomes suppressed upon further heating to 40K.

Following the discussion in Ref. [45], the strong anisotropy of the magnetic interaction modifies the overall aspect of the magnon dispersion. Instead of transversal low-energy magnons appearing at the AFM zone centers of the Brillouin zone soft excitations are expected at the zone boundaries of the AFM zigzag structure. Indeed, recent polarized INS studies on  $\alpha\text{-RuCl}_3$  revealed that the low-energy magnon commonly detected at the AFM zone center emerges unexpectedly in the longitudinal channel, i.e. polarized along the static moment direction [26]. Therefore, this spin-wave excitation cannot be explained as a transversal magnon but results from zone-

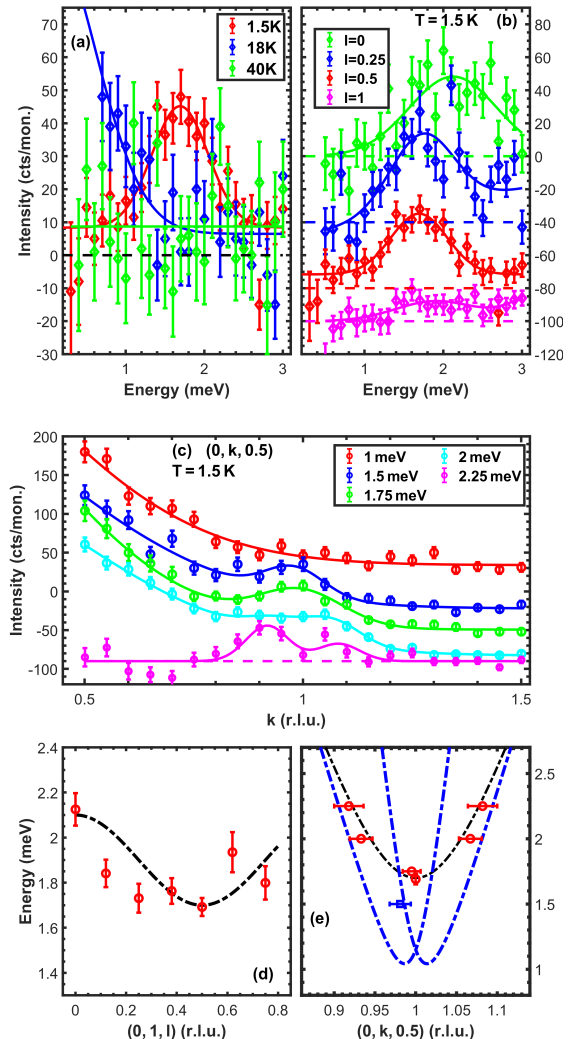


FIG. 3. INS results obtained on the cold TAS *Thales*: Constant- $\mathbf{Q}$  scans at the AFM zone center  $(0, 1, 0.5)$  at various temperatures, (a), and at  $(0, 1, l)$  for selected  $l$  values at  $T = 1.5$  K, (b). Background scans measured after rotating the sample by  $\pm 45^\circ$  are subtracted from the data. (c) Constant- $E$  scans across the AFM zone center at  $T = 1.5$  K. A background scan measured after rotating the sample by  $45^\circ$  has been subtracted from the data collected at  $E = 2.25$  meV, and the magenta dotted line indicates zero intensity. In panels (a-c), the monitor was set to  $4 \cdot 10^6$  counts and solid lines are Gaussian fits to the data, see main text. From these fits the magnon dispersion along the  $l$  (d) and the  $k$  (e) directions is drawn. Black dashed-dotted lines in panels (d,e) are guides to the eye, while the blue dashed-dotted lines in (e) indicate the calculated spin-wave dispersion. The square blue symbol refers to the data point collected at  $E = 1.5$  meV.

boundary modes that are folded to the AFM Bragg point due to the multi-domain arrangement inherent to the  $C_3$  symmetry of the honeycomb layer, see introduction. We thus emphasize that the signal and gap measured at the AFM zone center in  $\text{Na}_2\text{IrO}_3$  is not the common magnon anisotropy gap, but instead it is associated with the soft

excitations reflecting the non-condensed zigzag instabilities at the Brillouin zone boundaries ( $0.5, \pm 0.5, 0$ ).

To investigate the out-of-plane dispersion of this low-energy excitation, similar constant- $\mathbf{Q}$  scans at the 2D AFM zone centers  $(0, 1, l)$  with  $0 \leq l \leq 1$  have been collected at  $T = 1.5$  K, see Fig. 3(b). Background data sets are collected by performing similar energy scans after rotating the sample by  $\pm 45^\circ$  outside of any magnetic signal, and are subtracted from the data. The original data sets without background subtraction and some additional scans collected at other  $l$  values are shown in the Supplemental Material [54]. The magnon peak is fitted with a single Gaussian function. The  $l$  dependence of the energy gap, plotted in Fig. 3(d), is insignificant compared to the total energy range of magnetic excitations, which documents the 2D nature of the magnetic excitations, and the absence of sizable interlayer coupling. The dashed-dotted line is a guide to the eye using a cosine function  $a \cdot [\cos(2\pi k) + 1] + \Delta$ , where  $a = 0.2$  meV and  $\Delta = 1.7(1)$  meV.

We performed constant- $E$  scans across the AFM zone center  $(0, 1, \frac{1}{2})$  on *Thales* to study the in-plane magnon dispersion, see Fig. 3(c). While the scan at  $E = 1$  meV does not exhibit any peak, the magnon signal emerges at  $E = 1.5$  meV. At  $E = 2.25$  meV, because of the increase in background, a similar scan has been collected after rotating the sample by  $45^\circ$  where no magnetic signal is expected, and subtracted to the data set. For each data set below  $E = 2$  meV, background has been modeled by a Gaussian function centered at  $k = 0$ , and the magnon peaks dispersing from  $k = 1$  are modeled with a single or two symmetric Gaussian functions of equal width, for  $E \leq 1.75$  meV and  $E > 1.75$  meV, respectively. The Gaussian peak positions reported in Fig. 3(e) indicate the low-energy magnon dispersion. The dashed-dotted line is a guide to the eye using a parabolic dispersion, modeled with  $E = (\Delta^2 + c \cdot (k - 1)^2)^{0.5}$  ( $\Delta = 1.7(1)$  meV and  $c = 361$  meV $^2$ .r.l.u. $^{-2}$ ). Note that because of the finite resolution, the constant- $E$  scan at  $E = 1.5$  meV already senses the magnon dispersion and shows a magnetic signal in Fig. 3(c), while the energy gap is found at  $\Delta = 1.7(1)$  meV, see energy scan at  $T = 1.5$  K in Fig. 3(a).

The thermal TAS *IN8* permits studying the excitations at higher energy with higher neutron flux but broader resolution. At  $T = 1.5$  K, we performed constant-energy scans along  $(0, k, l)$  with  $l$  fixed. Neglecting all interlayer coupling, these scans cover the 2D AFM Bragg positions  $(0, 1, l)$ , denoted  $Y$  points, as well as the 2D FM positions  $(0, 0, l)$  corresponding to the 2D  $\Gamma$  points. While the chosen  $l$  values do not significantly impact the dispersion, they modify the absolute length of the scattering vector,  $|Q|$ , and thus the scattering angle, which determines the background. Background issues turned out crucial for these INS experiments due to the small amount of sample and the weak signal associated with a rapidly decaying form factor for a large  $5d$  magnetic ion.  $|Q|$  modifies the intensity of magnetic scattering through the square of the magnetic form factor. By tak-

ing out the sample we verified that a large part of the background did not stem from the sample but from the air and cryostat-material scattering as well as from rapid neutrons. This generates a background that for fixed energy transfer strongly increases toward low scattering angles or accordingly toward low  $|Q|$  values. Furthermore, reaching large  $E$  requires enhancing  $|Q|$  to close the scattering triangle,  $\mathbf{k}_i = \mathbf{Q} + \mathbf{k}_f$  (with  $\mathbf{k}_{i,f}$  the incoming and outgoing neutron momenta). In order to map the magnetic excitations that appear near  $(0, 1, l)$ , different  $l$  values must be studied.  $l = 0.5$  implies a large signal but also enhanced background, in particular when  $\mathbf{Q}$  approaches  $(0, 0, 0.5)$ , and it is not possible to study high energy transfer. In contrast scans at  $l = 1$  and  $1.5$  suffer less from the background variation but more from the reduced signal strength. The background conditions could be considerably improved in the second part *IN8(2)* of experiments using a different cryostat and tighter diaphragms, therefore we always specify which conditions apply.

Constant- $E$  scans at  $l = 0.5, 1$  and  $1.5$  across the 2D  $\Gamma$  and  $Y$  points are presented in Fig. 4 and Fig. 5 for the two experiments *IN8(1)* and *IN8(2)*, respectively. Magnon modes can be resolved up to  $E = 8, 10$ , and  $10$  meV for  $l = 0.5, 1$ , and  $1.5$ , respectively. The background is treated with a Gaussian function centered at  $k = 0$ , and the magnon peaks dispersing from  $k = 1$  are modeled with two Gaussian functions of equal width. At  $E = 2$  meV, only a single Gaussian peak is needed. These fits yield the dispersion data that are compared to the spin-wave calculations in Fig. 6. While the 2 meV signal can be easily studied at  $l = 0.5$ , higher energies require larger values,  $l = 1$  or  $1.5$ , to suppress the steeply rising background toward small scattering angle. Overall, the magnon dispersing away from the AFM zone center can be followed up to  $\sim 10$  meV. Already the first inspection reveals that the magnon dispersion is rather unusual as the signal remains centered close to the  $Y$  point at  $k = 1$  even for higher energies. The magnon  $k$  positions obtained for different  $l$  values in the two *IN8* experiments and those obtained at *Thales* are plotted together with the calculated magnon dispersion in Fig. 6(a), which illustrates the consistency of the three experiments.

Figure 4(e) presents energy scans for  $(0, 1, 0.5)$  and  $(0, 1, 1)$ , which show the low-energy response right at the 3D and 2D AFM zone centers, respectively, the stronger signal at  $l = 0.5$  can be attributed to the larger form factor and to the 3D ordering. In the first *IN8(1)* experiment we followed only the 2 meV signal as a function of temperature, see Fig 4(d). The large and temperature dependent background hampers a quantitative analysis, but correlations seem to persist well above  $T_N$ . Figure 5(d-f) presents temperature dependent data for higher energies and with the improved conditions of *IN8(2)*. The signal at 3 meV survives up to 100 K but it becomes significantly broadened indicating a shorter in-plane correlation length for these fluctuations. The signals at 6 and 8 meV also persist at 100 K and there is

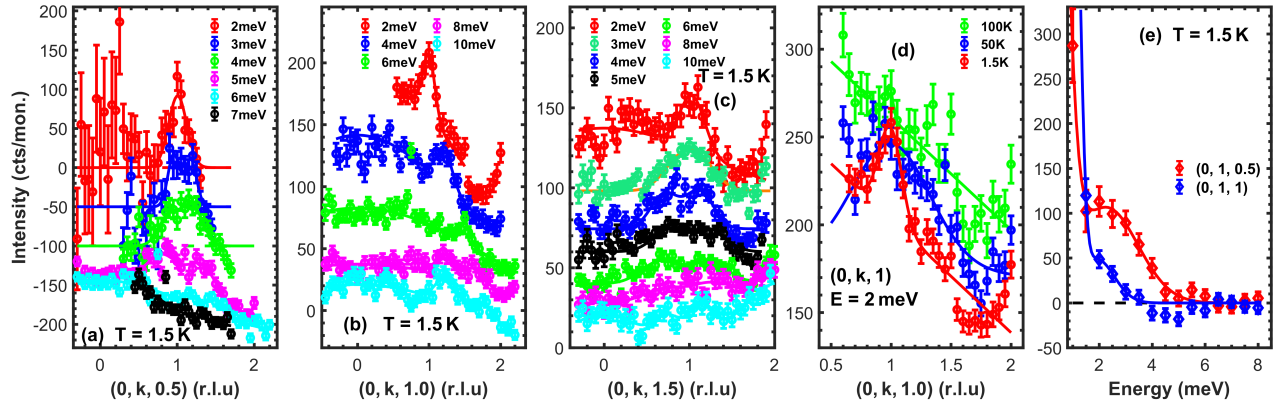


FIG. 4. Data obtained on IN8(1) normalized to  $2 \cdot 10^5$  monitor counts. Constant- $E$  scans across AFM zone centers at  $(0, 1, 0.5)$  (a),  $(0, 1, 1)$  (b) and  $(0, 1, 1.5)$  (c) at  $T = 1.5$  K (some data are vertically shifted [51]). In (a) background scans (collected after rotation of the sample by  $45^\circ$ ) have been subtracted from the data sets with  $E = 2, 3$  and  $4$  meV. Panel (d) compares the  $E = 2$  meV data for different temperatures. Panel (e) shows energy scans at the AFM zone centers  $(0, 1, 0.5)$  and  $(0, 1, 1)$  after subtraction of the background measured by rotating the sample by  $50^\circ$ .

no clear broadening, most likely because the signal is already broad at low temperature due to the superposition of  $k = 1 \pm \xi$  contributions. The observation of dynamic magnetic correlations to about 6 times  $T_N$  underlines the 2D nature of magnetic interactions and supports coupling parameters exceeding the simple energy scale given by  $T_N$ . Evidence for magnetic excitations at such temperatures was already deduced from RIXS studies [31, 33], but for much higher energies.

For  $\alpha$ -RuCl<sub>3</sub> various INS experiments revealed coexisting strong FM fluctuations that at high temperatures even become truly dominant [26, 32, 37, 40]. Similar fluctuations must become visible in our data covering not only the AFM scattering vectors  $(0, 1, l)$  but also the FM ones  $(0, 0, l)$ . The raw data, e.g. in Fig. 5(a), can suggest such a signal, but this enhanced intensity can be entirely attributed to the background that increases for small scattering angle and thus for small  $|Q|$ . In the first series of experiments IN8(1) we determined the background by repeating scans with the sample rotated by  $\pm 45^\circ$ . Fig. 4(a) presents the data after subtracting this background, which unambiguously shows that there is no comparably strong signal at the FM position. The data taken at  $l = 1.5$  and  $E = 6, 8$  and  $10$  meV in Fig. 4(c) confirm this conclusion for higher energies. Also the second part IN8(2) unambiguously shows the absence of such a FM signal for the entire energy range studied (between 2 and 9 meV), see Fig. 5(b,c). Constant- $E$  scans at  $(0, k, 1.5)$  have been repeated at  $E = 6, 8$ , and  $10$  meV with a larger neutron final wave vector  $k_f = 4.1 \text{ \AA}^{-1}$ , resulting in a larger resolution ellipsoid volume, thus strengthening the spectral weight of the hypothetical broad FM excitations. However, as shown in Fig. 5(c), there is no clear enhancement of the inelastic signal at  $k = 0$  underlining the absence of a strong FM signal in Na<sub>2</sub>IrO<sub>3</sub>. Note that the spin wave modes around  $k = 1$  appear as a broad signal and not as a sharp peak because of the worsened

energy resolution with  $k_f = 4.1 \text{ \AA}^{-1}$ . The increase at larger  $Q$  values results from crossing a low-lying optical phonon branch. Also the temperature dependent data in Fig. 5(d-f) do not indicate an enhancement of scattering at the FM positions. We thus conclude that the magnetic excitations in Na<sub>2</sub>IrO<sub>3</sub> fundamentally differ from those in  $\alpha$ -RuCl<sub>3</sub> by the absence of FM scattering in the low energy range of AFM magnons. Therefore, the latter cannot be taken as a clear indication of FM Kitaev interaction.

### C. LSWT Simulation

We analyze the magnon dispersion in Na<sub>2</sub>IrO<sub>3</sub> by LSWT applying one of the microscopic interaction models developed with the high-resolution RIXS data [33]. The spin-wave dispersion is computed with the package *spinW* [50] implementing the pure 2D interaction model in the honeycomb lattice in  $C2/m$  structure that is described by Equ. (1). Additional calculations inserting other published interaction-parameter sets are presented and discussed in the Supplemental Material [54]. While the INS data are insufficient to refine the magnetic interaction parameters of such complex models they extend the RIXS results toward the low-energy range and the magnon gap, which is crucial to evaluate these models.

The Curie-Weiss temperatures obtained from susceptibility measurements,  $\Theta_{\text{CW}\parallel} = -176$  K parallel to the layers and  $\Theta_{\text{CW}\perp} = -40$  K vertical, reflect the strong anisotropy of the material and indicate dominant AFM interactions [6, 14] but any quantitative interpretation must take the strong SOC into account. The zigzag magnetic order can be explained with a simple isotropic Heisenberg Hamiltonian including AFM exchange parameters up to the 3rd-nearest neighbors, and the corresponding spin wave dispersion could reproduce the dis-

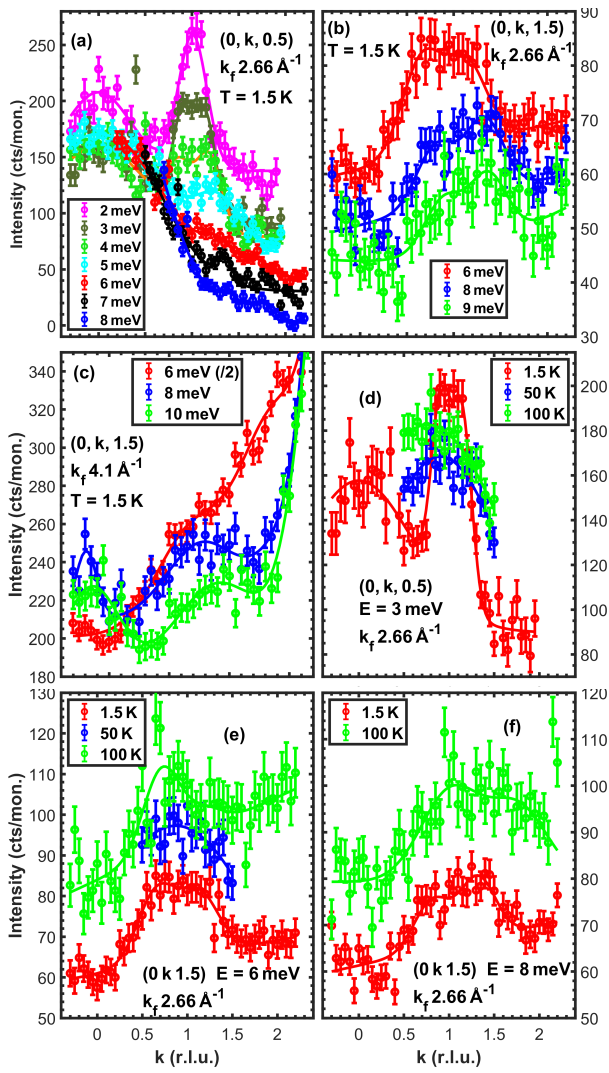


FIG. 5. Constant- $E$  scans along  $k$  direction obtained on IN8(2) normalized to  $2 \cdot 10^5$  monitor counts: across the AFM zone centers  $(0, 1, l)$  with  $l = 0.5$  (a) and  $l = 1.5$  (b), some data are shifted vertically [51]. Panel (c) shows constant- $E$  scans across  $(0, 1, 1.5)$  measured with a larger final energy,  $k_f = 4.1 \text{ \AA}^{-1}$ . Because of the high background, intensity of the 6 meV scan has been divided by a factor 2. Panels (d-f) show constant- $E$  scans (with  $k_f = 2.66 \text{ \AA}^{-1}$ ) for different temperatures. In all panels solid lines represent fits with Gaussian functions.

persive magnetic signal measured with powder INS [24]. However, as shown in the Supplemental Material [54], the computed spin wave dispersion cannot describe the experimental parabolic-like dispersion at low energy nor the peculiar high-energy dispersion deduced from the RIXS experiments [33].

The pure Kitaev model yields a QSL ground state. In order to stabilize the zigzag magnetic ground state and to describe the magnetic excitations, further couplings must be introduced leading to the commonly assumed  $HK\Gamma\Gamma'$  model presented in Eq. (1). The complexity

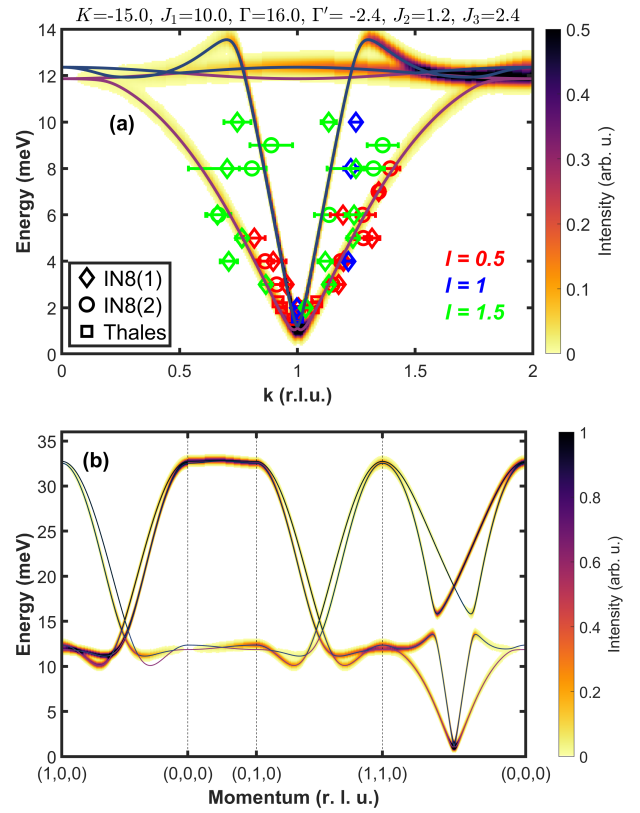


FIG. 6. Calculation of the spin-wave dispersion with the interaction parameters of model A3 in Ref. [33] and comparison with our experimental data (a) and computation of the spin wave dispersion along high symmetry directions (b). Only for panel (a) we superpose the contributions of the domains rotated by  $\pm 120^\circ$ , which is mandatory to compare with the experimental data. The title line gives the interaction parameters in meV.

of this model is considerable hampering an unambiguous determination of the parameters [33]. The orientation of the ordered moment can be used to restrict the parameter space, because the canting of the moment out of the layers depends sensitively on the ratios between  $J_1$ ,  $K$  and  $\Gamma$  [33, 41, 55]. However, the experimental precision of this canting angle [28] is limited and the interpretation is affected by the coupling of spin and orbital contributions. For  $\alpha$ -RuCl<sub>3</sub> polarized neutron diffraction finds a much lower canting compared to resonant x-ray diffraction, which can be at least partially attributed to different sensitivities of the two experimental techniques [26]. The RIXS data on Na<sub>2</sub>IrO<sub>3</sub> reveal magnetic excitations at the center of the Brillouin zone near 35 meV which fixes the overall interaction strength in Na<sub>2</sub>IrO<sub>3</sub> and which can discard many parameter sets, see Supplemental Material [54]. Two models labeled A2 and A3 were proposed in Ref. [33] to correctly describe the high-energy part of the magnetic excitation dispersion determined by RIXS. For these models little difference was found between LSWT and exact diagonalization calcula-

tions validating the LSWT approach. The two models though differ concerning the low-energy response, in particular model A2 shows some instability around the  $K$  point.

Fig. 6 presents the dispersion calculated with the parameter set of the  $HKT\Gamma'$  model labeled A3 in Ref. [33] that was implemented without any change. Panel (a) directly compares the calculated dispersion with our INS results and gives the numerical values of the interaction terms in the title line. Here, we sum over the calculated contributions from the three domains arising from the  $C_3$  symmetry of the honeycomb layer. Without any tuning of the parameters the agreement is good. The calculated dispersion well describes the low-energy magnon signal, that - we repeat - stems from the  $(0.5, \pm 0.5, l)$  propagation vectors of two rotated domains, but the experimental energy is slightly higher. The calculation also captures the low-energy dispersion of parabolic shape. The  $k$  positions determined at high energy that are close to 1 can be attributed to an additional branch. Since the model also describes the high-energy response observed in RIXS [33], there is no reason to further tune it. The full dispersion calculated for a single domain illustrates all the peculiarities of this model, see Fig. 6(b). There are no low-energy modes at the AFM zone center as discussed above and for  $\alpha\text{-RuCl}_3$  [26], which is a direct consequence of the bond-directional anisotropy. The steepest dispersion emerges along  $[1,0,0]$  which is parallel to the ferromagnetically arranged zigzag chains. Again this perfectly reflects the situation in  $\alpha\text{-RuCl}_3$ . There is, however, an important difference between the  $\text{Na}_2\text{IrO}_3$  dispersion presented in Fig. 6 and that in  $\alpha\text{-RuCl}_3$ .  $\text{Na}_2\text{IrO}_3$  does not exhibit a FM instability, as there are no soft magnon excitations near the FM zone center, while  $\alpha\text{-RuCl}_3$  exhibits at low temperature a strong mode at 2 meV that furthermore is very sharp [26, 36–38]. Also at higher energy up to  $\sim 9$  meV  $\text{Na}_2\text{IrO}_3$  does not exhibit a FM signal of comparable strength to the AFM magnon neither at 1.5 K nor at higher temperature. The presented interaction model for  $\text{Na}_2\text{IrO}_3$  perfectly captures this finding, see Fig. 6; such a FM mode is thus not a direct consequence of the FM Kitaev parameter. Instead it must be attributed to the FM  $J_1$  interaction of  $\alpha\text{-RuCl}_3$  that is AFM in  $\text{Na}_2\text{IrO}_3$  [33], as it has been also deduced from theoretical estimations of the interaction parameters [56].

The absence of the FM instability in our neutron data on  $\text{Na}_2\text{IrO}_3$  and the strength of such excitations in  $\alpha\text{-RuCl}_3$  [26, 32, 36, 37, 40] indicate the important qualitative difference of the magnetic interactions in these two materials. While in both compounds the FM Kitaev term is strong qualifying them unambiguously as Kitaev materials, there are other terms of comparable size, in particular  $\Gamma$  and  $J_1$ . The sign change of  $J_1$  between the two materials results in quite different nearest neighbor interaction matrices. For  $\alpha\text{-RuCl}_3$  the strongest eigenvalue still corresponds to the initial Kitaev term (using the set of parameters discussed in [26]) but the two other Eigenvalues are of comparable size. With the  $\text{Na}_2\text{IrO}_3$

model discussed above, there is one dominating eigenvalue that, however, corresponds to the  $[011]$  direction for the  $X$  bond. Both materials thus considerably deviate from the ideal Kitaev model, but in quite different ways. Whether it is still possible to observe signatures of the ideal Kitaev model in these materials remains an open challenge, but the deviations from Kitaev physics must be different in these two best characterized Kitaev candidate materials.

#### IV. CONCLUSION

We report on neutron scattering analyses of  $\text{Na}_2\text{IrO}_3$  studying a sample consisting of 63 co-aligned crystals. Magnetic superstructure reflections appear below  $T_N = 15$  K and indicate magnetic order that is well defined perpendicular to the layers. However, there is also quasistatic diffuse scattering indicating correlations with shorter coherence along  $\mathbf{c}^*$  and magnetic stacking faults.

High-resolution INS scans indicate a small magnon gap of 1.7(1) meV, which closely resembles the finding in  $\alpha\text{-RuCl}_3$ . In analogy and in agreement with the LSWT calculation, this low-energy mode does not correspond to the usual transversal magnon at AFM zone center but stems from the zone boundary modes of the two domains rotated by  $\pm 120^\circ$  against the domain that contributes to the magnetic Bragg scattering. This mode shows almost no dispersion perpendicular to the layers confirming the pronounced 2D nature of magnetic interactions in  $\text{Na}_2\text{IrO}_3$ . By scanning with fixed energy transfer along  $(0, 1 \pm \xi, l)$  we determine the low-energy part of the magnon dispersion, which complements the earlier RIXS studies at higher energies. There is a non-trivial dispersion with some steepening of the dispersion towards higher energies. The comparison of the measured dispersion with LSWT implementing interaction parameters deduced from high-energy RIXS data [33] yields satisfactory agreement without any tuning of parameters corroborating this model. The parameter set supports strong Kitaev interaction for  $\text{Na}_2\text{IrO}_3$  that is, however, not dominating.

The dispersion of magnetic excitations in  $\text{Na}_2\text{IrO}_3$  and in  $\alpha\text{-RuCl}_3$  resembles each other concerning the low-energy mode stemming from the zone-boundary instability and the parabola-shaped dispersion, that are both captured by the  $HKT\Gamma'$  models for the two systems. There is however an important difference concerning the FM instability.  $\alpha\text{-RuCl}_3$  exhibits low-energy and very sharp modes at the 2D FM zone centers and this response even dominates the spectrum at higher temperatures. In  $\text{Na}_2\text{IrO}_3$  we do not find such a signal in spite of strong efforts in the energy range 2 to 9 meV where we can unambiguously detect the magnon dispersion near the AFM positions. As it has been already deduced from theoretical analyses [56],  $\text{Na}_2\text{IrO}_3$  differs from its  $\alpha\text{-RuCl}_3$  sister compound concerning the absence of a FM instability in spite of both materials exhibiting a FM Kitaev term.

The nearest-neighbor Heisenberg term, however, is FM in  $\alpha$ -RuCl<sub>3</sub> but AFM in Na<sub>2</sub>IrO<sub>3</sub>.

## ACKNOWLEDGMENTS

AB and MB acknowledge funding from the Deutsche Forschungsgemeinschaft (DFG, German Research Foun-

dation) under CRC 1238-277146847 (subproject B04). G.C. acknowledges the US National Science Foundation support via Grant No. DMR 2204811.

## DATA AVAILABILITY

The data that support the findings of this article are openly available [57].

---

[1] Z. Nussinov and J. van den Brink, Compass models: Theory and physical motivations, *Rev. Mod. Phys.* **87**, 1 (2015).

[2] A. Kitaev, Anyons in an exactly solved model and beyond, *Annals of Physics* **321**, 2 (2006), january Special Issue.

[3] C. Nayak, S. H. Simon, A. Stern, M. Freedman, and S. Das Sarma, Non-Abelian anyons and topological quantum computation, *Rev. Mod. Phys.* **80**, 1083 (2008).

[4] G. Jackeli and G. Khaliullin, Mott Insulators in the Strong Spin-Orbit Coupling Limit: From Heisenberg to a Quantum Compass and Kitaev Models, *Phys. Rev. Lett.* **102**, 017205 (2009).

[5] J. Chaloupka, G. Jackeli, and G. Khaliullin, Kitaev-Heisenberg Model on a Honeycomb Lattice: Possible Exotic Phases in Iridium Oxides  $A_2\text{IrO}_3$ , *Phys. Rev. Lett.* **105**, 027204 (2010).

[6] Y. Singh and P. Gegenwart, Antiferromagnetic Mott insulating state in single crystals of the honeycomb lattice material Na<sub>2</sub>IrO<sub>3</sub>, *Phys. Rev. B* **82**, 064412 (2010).

[7] Y. Singh, S. Manni, J. Reuther, T. Berlijn, R. Thomale, W. Ku, S. Trebst, and P. Gegenwart, Relevance of the Heisenberg-Kitaev Model for the Honeycomb Lattice Iridates  $A_2\text{IrO}_3$ , *Phys. Rev. Lett.* **108**, 127203 (2012).

[8] K. Plumb, J. Clancy, L. Sandilands, V. V. Shankar, Y. Hu, K. Burch, H.-Y. Kee, and Y.-J. Kim,  $\alpha$ -RuCl<sub>3</sub>: A spin-orbit assisted Mott insulator on a honeycomb lattice, *Phys. Rev. B* **90**, 041112 (2014).

[9] W. Witczak-Krempa, G. Chen, Y. B. Kim, and L. Balents, Correlated quantum phenomena in the strong spin-orbit regime, *Annu. Rev. Condens. Matter Phys.* **5**, 57 (2014).

[10] R. Schaffer, E. K.-H. Lee, B.-J. Yang, and Y. B. Kim, Recent progress on correlated electron systems with strong spin-orbit coupling, *Reports on Progress in Physics* **79**, 094504 (2016).

[11] J. G. Rau, E. K.-H. Lee, and H.-Y. Kee, Spin-Orbit Physics Giving Rise to Novel Phases in Correlated Systems: Iridates and Related Materials, *Annual Review of Condensed Matter Physics* **7**, 195 (2016).

[12] G. Cao and P. Schlottmann, The challenge of spin-orbit-tuned ground states in iridates: a key issues review, *Reports on Progress in Physics* **81**, 042502 (2018).

[13] S. M. Winter, A. A. Tsirlin, M. Daghofer, J. van den Brink, Y. Singh, P. Gegenwart, and R. Valentí, Models and materials for generalized Kitaev magnetism, *Journal of Physics: Condensed Matter* **29**, 493002 (2017).

[14] H. Takagi, T. Takayama, G. Jackeli, G. Khaliullin, and S. E. Nagler, Concept and realization of kitaev quantum spin liquids, *Nature Reviews Physics* **1**, 264 (2019).

[15] H. Liu, J. Chaloupka, and G. Khaliullin, Kitaev Spin Liquid in 3d Transition Metal Compounds, *Phys. Rev. Lett.* **125**, 047201 (2020).

[16] Y. Motome, R. Sano, S. Jang, Y. Sugita, and Y. Kato, Materials design of Kitaev spin liquids beyond the Jackeli-Khaliullin mechanism, *Journal of Physics: Condensed Matter* **32**, 404001 (2020).

[17] S. Trebst and C. Hickey, Kitaev materials, *Physics Reports* **950**, 1 (2022).

[18] I. Rousochatzakis, N. B. Perkins, Q. Luo, and H.-Y. Kee, Beyond Kitaev physics in strong spin-orbit coupled magnets, *Reports on Progress in Physics* **87**, 026502 (2024).

[19] S.-H. Jang and Y. Motome, Exchange Interactions in Rare-earth Magnets  $A_2\text{PrO}_3$  ( $A$ = alkali metals): Revised (2024), arXiv:2404.17058 [cond-mat.str-el].

[20] B. J. Kim, H. Jin, S. J. Moon, J.-Y. Kim, B.-G. Park, C. S. Leem, J. Yu, T. W. Noh, C. Kim, S.-J. Oh, J.-H. Park, V. Durairaj, G. Cao, and E. Rotenberg, Novel  $J_{\text{eff}} = 1/2$  Mott State Induced by Relativistic Spin-Orbit Coupling in Sr<sub>2</sub>IrO<sub>4</sub>, *Phys. Rev. Lett.* **101**, 076402 (2008).

[21] B. J. Kim, H. Ohsumi, T. Komesu, S. Sakai, T. Morita, H. Takagi, and T. Arima, Phase-Sensitive Observation of a Spin-Orbital Mott State in Sr<sub>2</sub>IrO<sub>4</sub>, *Science* **323**, 1329 (2009).

[22] R. Comin, G. Levy, B. Ludbrook, Z.-H. Zhu, C. N. Veenstra, J. A. Rosen, Y. Singh, P. Gegenwart, D. Stricker, J. N. Hancock, D. van der Marel, I. S. Elfimov, and A. Damascelli, Na<sub>2</sub>IrO<sub>3</sub> as a Novel Relativistic Mott Insulator with a 340-meV Gap, *Phys. Rev. Lett.* **109**, 266406 (2012).

[23] A. Shitade, H. Katsura, J. Kuneš, X.-L. Qi, S.-C. Zhang, and N. Nagaosa, Quantum Spin Hall Effect in a Transition Metal Oxide Na<sub>2</sub>IrO<sub>3</sub>, *Phys. Rev. Lett.* **102**, 256403 (2009).

[24] S. K. Choi, R. Coldea, A. N. Kolmogorov, T. Lancaster, I. I. Mazin, S. J. Blundell, P. G. Radaelli, Y. Singh, P. Gegenwart, K. R. Choi, S.-W. Cheong, P. J. Baker, C. Stock, and J. Taylor, Spin Waves and Revised Crystal Structure of Honeycomb Iridate Na<sub>2</sub>IrO<sub>3</sub>, *Phys. Rev. Lett.* **108**, 127204 (2012).

[25] F. Ye, S. Chi, H. Cao, B. C. Chakoumakos, J. A. Fernandez-Baca, R. Custelcean, T. F. Qi, O. B. Korneta, and G. Cao, Direct evidence of a zigzag spin-chain structure in the honeycomb lattice: A neutron and x-ray diffraction investigation of single-crystal Na<sub>2</sub>IrO<sub>3</sub>, *Phys. Rev. B* **85**, 180403 (2012).

[26] M. Braden, X. Wang, A. Bertin, P. Steffens, and Y. Su, Direct Evidence for Anisotropic Magnetic Interaction in  $\alpha$ -RuCl<sub>3</sub> from Polarized Inelastic Neutron Scattering, *Phys. Rev. Lett.* **134**, 236702 (2025).

[27] X. Liu, T. Berlijn, W.-G. Yin, W. Ku, A. Tsvelik, Y.-J.

Kim, H. Gretarsson, Y. Singh, P. Gegenwart, and J. P. Hill, Long-range magnetic ordering in  $\text{Na}_2\text{IrO}_3$ , *Phys. Rev. B* **83**, 220403 (2011).

[28] S. Hwan Chun, J.-W. Kim, J. Kim, H. Zheng, C. C. Stoumpos, C. Malliakas, J. Mitchell, K. Mehlawat, Y. Singh, Y. Choi, *et al.*, Direct evidence for dominant bond-directional interactions in a honeycomb lattice iridate  $\text{Na}_2\text{IrO}_3$ , *Nature Physics* **11**, 462 (2015).

[29] K. Mehlawat, A. Thamizhavel, and Y. Singh, Heat capacity evidence for proximity to the Kitaev quantum spin liquid in  $A_2\text{IrO}_3$  ( $A = \text{Na}, \text{Li}$ ), *Phys. Rev. B* **95**, 144406 (2017).

[30] H. Gretarsson, J. P. Clancy, Y. Singh, P. Gegenwart, J. P. Hill, J. Kim, M. H. Upton, A. H. Said, D. Casa, T. Gog, and Y.-J. Kim, Magnetic excitation spectrum of  $\text{Na}_2\text{IrO}_3$  probed with resonant inelastic x-ray scattering, *Phys. Rev. B* **87**, 220407 (2013).

[31] A. Revelli, M. M. Sala, G. Monaco, C. Hickey, P. Becker, F. Freund, A. Jesche, P. Gegenwart, T. Eschmann, F. Buessen, *et al.*, Fingerprints of Kitaev physics in the magnetic excitations of honeycomb iridates, *Phys. Rev. Res.* **2**, 043094 (2020).

[32] A. Banerjee, J. Yan, J. Knolle, C. A. Bridges, M. B. Stone, M. D. Lumsden, D. G. Mandrus, D. A. Tennant, R. Moessner, and S. E. Nagler, Neutron scattering in the proximate quantum spin liquid  $\alpha\text{-RuCl}_3$ , *Science* **356**, 1055 (2017).

[33] J. Kim, J. Chaloupka, Y. Singh, J. W. Kim, B. J. Kim, D. Casa, A. Said, X. Huang, and T. Gog, Dynamic Spin Correlations in the Honeycomb Lattice  $\text{Na}_2\text{IrO}_3$  Measured by Resonant Inelastic x-Ray Scattering, *Phys. Rev. X* **10**, 021034 (2020).

[34] M. Magnaterra, K. Hopfer, C. J. Sahle, M. M. Sala, G. Monaco, J. Attig, C. Hickey, I. M. Pietsch, F. Breitner, P. Gegenwart, M. H. Upton, J. Kim, S. Trebst, P. H. M. van Loosdrecht, J. van den Brink, and M. Grüninger, RIXS observation of bond-directional nearest-neighbor excitations in the Kitaev material  $\text{Na}_2\text{IrO}_3$  (2023), arXiv:2301.08340 [cond-mat.str-el].

[35] A. Banerjee, C. Bridges, J.-Q. Yan, A. Aczel, L. Li, M. Stone, G. Granroth, M. Lumsden, Y. Yiu, J. Knolle, *et al.*, Proximate Kitaev quantum spin liquid behaviour in a honeycomb magnet, *Nature materials* **15**, 733 (2016).

[36] A. Banerjee, P. Lampen-Kelley, J. Knolle, C. Balz, A. A. Aczel, B. Winn, Y. Liu, D. Pajerowski, J. Yan, C. A. Bridges, *et al.*, Excitations in the field-induced quantum spin liquid state of  $\alpha\text{-RuCl}_3$ , *npj Quantum Materials* **3**, 8 (2018).

[37] C. Balz, P. Lampen-Kelley, A. Banerjee, J. Yan, Z. Lu, X. Hu, S. M. Yadav, Y. Takano, Y. Liu, D. A. Tennant, M. D. Lumsden, D. Mandrus, and S. E. Nagler, Finite field regime for a quantum spin liquid in  $\alpha\text{-RuCl}_3$ , *Phys. Rev. B* **100**, 060405 (2019).

[38] K. Ran, J. Wang, W. Wang, Z.-Y. Dong, X. Ren, S. Bao, S. Li, Z. Ma, Y. Gan, Y. Zhang, *et al.*, Spin-Wave Excitations Evidencing the Kitaev Interaction in Single Crystalline  $\alpha\text{-RuCl}_3$ , *Phys. Rev. Lett.* **118**, 107203 (2017).

[39] K. Ran, J. Wang, S. Bao, Z. Cai, Y. Shangguan, Z. Ma, W. Wang, Z.-Y. Dong, P. Čermák, A. Schneidewind, S. Meng, Z. Lu, S.-L. Yu, J.-X. Li, and J. Wen, Evidence for Magnetic Fractional Excitations in a Kitaev Quantum-Spin-Liquid Candidate  $\alpha\text{-RuCl}_3$ , *Chinese Physics Letters* **39**, 027501 (2022).

[40] S.-H. Do, S.-Y. Park, J. Yoshitake, J. Nasu, Y. Motome, Y. S. Kwon, D. Adroja, D. Voneshen, K. Kim, T.-H. Jang, *et al.*, Majorana fermions in the Kitaev quantum spin system  $\alpha\text{-RuCl}_3$ , *Nature Physics* **13**, 1079 (2017).

[41] M. Möller, P. A. Maksimov, S. Jiang, S. R. White, R. Valentí, and A. L. Chernyshev, Rethinking  $\alpha\text{-RuCl}_3$ : Parameters, models, and phase diagram, *Phys. Rev. B* **112**, 104403 (2025).

[42] K. Foyevtsova, H. O. Jeschke, I. I. Mazin, D. I. Khomskii, and R. Valentí, Ab initio analysis of the tight-binding parameters and magnetic interactions in  $\text{Na}_2\text{IrO}_3$ , *Phys. Rev. B* **88**, 035107 (2013).

[43] V. M. Katukuri, S. Nishimoto, V. Yushankhai, A. Stoyanova, H. Kandpal, S. Choi, R. Coldea, I. Rousochatzakis, L. Hozoi, and J. Van Den Brink, Kitaev interactions between  $j = 1/2$  moments in honeycomb  $\text{Na}_2\text{IrO}_3$  are large and ferromagnetic: insights from ab initio quantum chemistry calculations, *New Journal of Physics* **16**, 013056 (2014).

[44] J. Chaloupka, G. Jackeli, and G. Khaliullin, Zigzag Magnetic Order in the Iridium Oxide  $\text{Na}_2\text{IrO}_3$ , *Phys. Rev. Lett.* **110**, 097204 (2013).

[45] J. Chaloupka and G. Khaliullin, Hidden symmetries of the extended Kitaev-Heisenberg model: Implications for the honeycomb-lattice iridates  $A_2\text{IrO}_3$ , *Phys. Rev. B* **92**, 024413 (2015).

[46] Piovano, Andrea and Ivanov, Alexandre, The tas-in8 upgrade: Towards the limit of a three-axis spectrometer performance, *EPJ Web Conf.* **286**, 03011 (2023).

[47] K. Jenni, A. Bertin, S. Biesenkamp, M. Braden, and A. Ivanov, (2020), Magnetic excitations in  $\text{Na}_2\text{IrO}_3$ . Institut Laue-Langevin (ILL) doi:10.5291/ILL-DATA.4-05-759.

[48] A. Bertin, M. Braden, and A. Ivanov, (2020), Kitaev excitations and magnons temperature behaviour in  $\text{Na}_2\text{IrO}_3$ . Institut Laue-Langevin (ILL) doi:10.5291/ILL-DATA.4-05-790.

[49] A. Bertin, M. Braden, and P. Steffens, (2020), Anisotropy gap in the magnon dispersion of  $\text{Na}_2\text{IrO}_3$ . Institut Laue-Langevin (ILL) doi:10.5291/ILL-DATA.4-05-791.

[50] S. Toth and B. Lake, Linear spin wave theory for single-q incommensurate magnetic structures, *Journal of Physics: Condensed Matter* **27**, 166002 (2015).

[51] In Fig. 2(b) and (c), data collected at  $T = 5, 7, 9, 11, 13, 15, 16\text{ K}$  have been shifted by  $-40, -80, -120, -160, -200, -240, -280\text{ cts/s}$ , respectively. In Fig. 3(b) data at  $l = 0.25, 0.5, 1$  are shifted by  $-40, -80, -100\text{ cts/mon.}$ , respectively. In Fig. 3(c) data at  $E = 1.5, 1.75, 2, 2.25\text{ meV}$  are shifted by  $-50, -100, -150, -350\text{ cts/mon.}$ , respectively. In Fig. 4(a) the data collected at  $E = 3, 4, 5, 6, 7\text{ meV}$  have been shifted by  $-50, -100, -300, -300, -300\text{ cts/mon.}$ , respectively; in Fig. 4(b) data collected at  $E = 2, 4, 6, 8, 10\text{ meV}$  have been shifted by  $-50, -20, -40, -60, -90\text{ cts/mon.}$ , and in Fig. 4(c) data collected at  $E = 2, 4, 5, 6, 8, 10\text{ meV}$  by  $-20, -10, -20, -30, -40, -60\text{ cts/mon.}$ , respectively. In Fig. 5(a) the  $E = 6, 7, 8\text{ meV}$  data are vertically shifted by  $-20, -40, -60\text{ cts/mon.}$ , and in Fig. 5(b) data at  $E = 8, 9\text{ meV}$  are shifted by  $-10, -20\text{ cts/mon.}$ , respectively..

[52] Le Guillou, J.C. and Zinn-Justin, J., Accurate critical exponents for ising like systems in non-integer dimensions, *J. Phys. France* **48**, 19 (1987).

[53] M. A. Novotny, Critical exponents for the ising model between one and two dimensions, *Phys. Rev. B* **46**, 2939

(1992).

[54] Supplemental Material reporting on additional INS data and on linear spin-wave theory calculations is given in \*\*\*\*; the discussion invokes the references [5, 24, 28, 33, 41–45, 50, 55, 56, 58–74].

[55] J. Chaloupka and G. Khaliullin, Magnetic anisotropy in the Kitaev model systems  $\text{Na}_2\text{IrO}_3$  and  $\text{RuCl}_3$ , Phys. Rev. B **94**, 064435 (2016).

[56] H. Liu, J. Chaloupka, and G. Khaliullin, Exchange interactions in  $d^5$  Kitaev materials: From  $\text{Na}_2\text{IrO}_3$  to  $\alpha\text{-RuCl}_3$ , Phys. Rev. B **105**, 214411 (2022).

[57] A. Bertin, H. Zhao, G. Cao, A. Piovano, P. Steffens, A. Ivanov and M. Braden, Data Supporting "Magnetic excitations in the Kitaev material  $\text{Na}_2\text{IrO}_3$  studied by neutron scattering" by A. Bertin et al., 10.5281/zenodo.18622556. (2026).

[58] Y. Yamaji, Y. Nomura, M. Kurita, R. Arita, and M. Imada, First-Principles Study of the Honeycomb-Lattice Iridates  $\text{Na}_2\text{IrO}_3$  in the Presence of Strong Spin-Orbit Interaction and Electron Correlations, Phys. Rev. Lett. **113**, 107201 (2014).

[59] S. M. Winter, Y. Li, H. O. Jeschke, and R. Valentí, Challenges in design of Kitaev materials: Magnetic interactions from competing energy scales, Phys. Rev. B **93**, 214431 (2016).

[60] Y. S. Hou, J. H. Yang, H. J. Xiang, and X. G. Gong, First-principles study of the magnetic interactions in honeycomb  $\text{Na}_2\text{IrO}_3$ , Phys. Rev. B **98**, 094401 (2018).

[61] J. Reuther, R. Thomale, and S. Trebst, Finite-temperature phase diagram of the Heisenberg-Kitaev model, Phys. Rev. B **84**, 100406 (2011).

[62] C. Price and N. B. Perkins, Finite-temperature phase diagram of the classical Kitaev-Heisenberg model, Phys. Rev. B **88**, 024410 (2013).

[63] J. Osorio Iregui, P. Corboz, and M. Troyer, Probing the stability of the spin-liquid phases in the Kitaev-Heisenberg model using tensor network algorithms, Phys. Rev. B **90**, 195102 (2014).

[64] D. Gotfryd, J. Rusnáčko, K. Wohlfeld, G. Jackeli, J. c. v. Chaloupka, and A. M. Oleš, Phase diagram and spin correlations of the Kitaev-Heisenberg model: Importance of quantum effects, Phys. Rev. B **95**, 024426 (2017).

[65] I. Kimchi and Y.-Z. You, Kitaev-Heisenberg- $J_2$ - $J_3$  model for the iridates  $\text{A}_2\text{IrO}_3$ , Phys. Rev. B **84**, 180407 (2011).

[66] J. G. Rau, E. K.-H. Lee, and H.-Y. Kee, Generic Spin Model for the Honeycomb Iridates beyond the Kitaev Limit, Phys. Rev. Lett. **112**, 077204 (2014).

[67] Y. Sizyuk, C. Price, P. Wölfle, and N. B. Perkins, Importance of anisotropic exchange interactions in honeycomb iridates: Minimal model for zigzag antiferromagnetic order in  $\text{Na}_2\text{IrO}_3$ , Phys. Rev. B **90**, 155126 (2014).

[68] J. G. Rau and H.-Y. Kee, Trigonal distortion in the honeycomb iridates: Proximity of zigzag and spiral phases in  $\text{Na}_2\text{IrO}_3$  (2014), arXiv:1408.4811 [cond-mat.str-el].

[69] H. Gretarsson, J. P. Clancy, X. Liu, J. P. Hill, E. Bozin, Y. Singh, S. Manni, P. Gegenwart, J. Kim, A. H. Said, D. Casa, T. Gog, M. H. Upton, H.-S. Kim, J. Yu, V. M. Katukuri, L. Hozoi, J. van den Brink, and Y.-J. Kim, Crystal-Field Splitting and Correlation Effect on the Electronic Structure of  $\text{A}_2\text{IrO}_3$ , Phys. Rev. Lett. **110**, 076402 (2013).

[70] M. A. Tovar-Olvera, P. Ruiz-Díaz, and M. Saubanère, Influence of local structural distortion on the magnetism of  $\text{Na}_2\text{IrO}_3$  compounds, Phys. Rev. B **105**, 094413 (2022).

[71] P. Yadav, S. Sarkar, M. Sharma, D. M. Phase, R. J. Choudhary, and R. Raghunathan, Role of Local Structural Distortions on the Origin of  $j = 1/2$  Pseudo-Spin State in Sodium Iridate, ACS Applied Electronic Materials **5**, 418 (2023).

[72] I. Rousouchatzakis, J. Reuther, R. Thomale, S. Rachel, and N. B. Perkins, Phase Diagram and Quantum Order by Disorder in the Kitaev  $K_1 - K_2$  Honeycomb Magnet, Phys. Rev. X **5**, 041035 (2015).

[73] Y. Sizyuk, P. Wölfle, and N. B. Perkins, Selection of direction of the ordered moments in  $\text{Na}_2\text{IrO}_3$  and  $\alpha\text{-RuCl}_3$ , Phys. Rev. B **94**, 085109 (2016).

[74] Y. Yamaji, T. Suzuki, T. Yamada, S.-I. Suga, N. Kawashima, and M. Imada, Clues and criteria for designing a Kitaev spin liquid revealed by thermal and spin excitations of the honeycomb iridate  $\text{Na}_2\text{IrO}_3$ , Phys. Rev. B **93**, 174425 (2016).